FISEVIER

Contents lists available at ScienceDirect

# Science of the Total Environment

journal homepage: www.elsevier.com/locate/scitotenv



# PanoMRT: Panoramic infrared thermography to model human thermal exposure and comfort



Ariane Middel a,b,\*, Matthew Huff b, E. Scott Krayenhoff c, Ananth Udupa d, Florian A. Schneider e

- <sup>a</sup> School of Arts, Media and Engineering, Arizona State University, USA
- <sup>b</sup> School of Computing and Augmented Intelligence, Arizona State University, USA
- <sup>c</sup> School of Environmental Sciences, University of Guelph, Canada
- <sup>d</sup> The Design School, Arizona State University, USA
- e School of Sustainability, Arizona State University, USA

#### HIGHLIGHTS

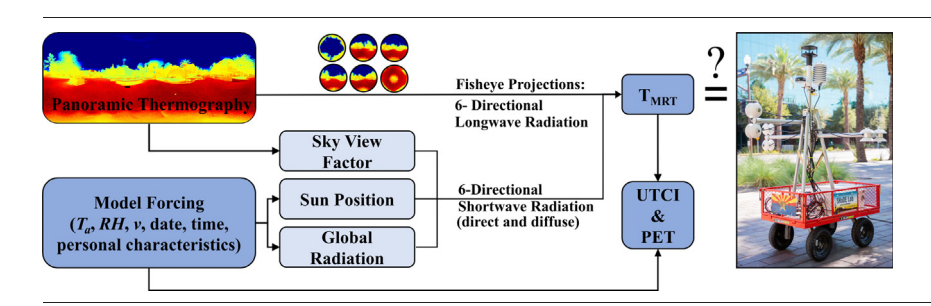
- PanoMRT calculates outdoor thermal exposure and comfort from panoramic infrared thermography.
- Surface temperatures in cities vary widely due to heterogeneous materials and shade patterns.
- 3D surface temperature information significantly improves mean radiant temperature models.

## ARTICLE INFO

Editor: Scott Sheridan

Keywords:
Thermal exposure
Mean radiant temperature
Infrared thermal panoramas
Human-biometeorological observations and
modeling

## GRAPHICAL ABSTRACT



## ABSTRACT

As summer heat waves become the new normal worldwide, modeling human thermal exposure and comfort to assess and mitigate urban overheating is crucial to uphold livability in cities. We introduce PanoMRT, an open source humanbiometeorological model to calculate Mean Radiant Temperature  $(T_{MRT})$ , Physiologically Equivalent Temperature (PET), and the Universal Thermal Climate Index (UTCI) from thermal equirectangular 360° panoramas and standard weather information (air temperature, relative humidity, wind speed). We validated the model for hot, dry, clear summer days in Tempe, Arizona, USA with in-situ observations using a FLIR Duo Pro R thermal camera on a rotating arm and the mobile human-biometeorological instrument platform MaRTy. We observed and modeled  $T_{MRT}$  and thermal comfort for 19 sites with varying ground cover (grass, concrete, asphalt), sky view factor, exposure (sun, shade), and shade type (engineered, natural) six times per day. PanoMRT performed well with a Root Mean Square Error (RMSE) of 4.1 °C for  $T_{MRT}$ , 2.6 °C for PET, and 1.2 °C for UTCI, meeting the accuracy requirement of  $\pm 5$  °C set in the ISO 7726 standard for heat and cold stress studies. RayMan reference model runs without measured surface temperature forcing reveal that accurate longwave radiative flux estimations are crucial to meet the  $\pm 5$  °C threshold, particularly for shaded locations and during midday when surface temperatures peak and longwave modeling errors are largest. This study demonstrates the importance of spatially resolved 3D surface temperature data for thermal exposure and comfort modeling to capture complex longwave radiation exposure patterns resulting from heterogeneity in built configuration and material radiative and thermal properties in the built environment.

E-mail addresses: ariane.middel@asu.edu (A. Middel), mwhuff@asu.edu (M. Huff), skrayenh@uoguelph.ca (E.S. Krayenhoff), audupa@asu.edu (A. Udupa), florian.schneider@asu.edu (F.A. Schneider).

#### http://dx.doi.org/10.1016/j.scitotenv.2022.160301

Received 16 August 2022; Received in revised form 25 October 2022; Accepted 15 November 2022 Available online 18 November 2022

0048-9697/© 2022 The Authors. Published by Elsevier B.V. This is an open access article under the CC BY-NC-ND license (http://creativecommons.org/licenses/by-nc-nd/4.0/).

<sup>\*</sup> Corresponding author at: School of Arts, Media and Engineering, School of Computing and Augmented Intelligence, Arizona State University, 950 S. Forest Mall, Stauffer B, Tempe, AZ 85281, USA.

## **Abbreviations**

```
atmospheric radiation [Wm<sup>-2</sup>]
\boldsymbol{A}
            diffuse shortwave radiation [Wm<sup>-2</sup>]
D
            isotropic diffuse shortwave radiation [Wm<sup>-2</sup>]
D_{iso}
            anisotropic diffuse shortwave radiation [\mathrm{Wm}^{-2}]
Daniso
f_{SVF}
            sky view factor [ – ]
            angular weighting factor for standing reference person for
            radiation incident from direction i (0.22 for N, E, S, W; 0.06 for
            up/down)[-]
            global shortwave radiation, f_{SVF} = 1, cloudless [Wm<sup>-2</sup>]
G_0
            index that denotes directions (N, E, S, W, up, down)
i
            direct shortwave radiation on a horizontal surface [Wm<sup>-2</sup>]
I
ľ
            direct shortwave radiation on a surface perpendicular to the
            Sun [Wm<sup>-2</sup>]
            solar constant (1367) [Wm^{-2}]
\overline{I}_0
            extraterrestrial radiation [Wm<sup>-2</sup>]
            directional shortwave radiation (i denotes N, E, S, W, up, down)
K_i
K_{\downarrow}, K_{\uparrow}, K_{\rightarrow} directional shortwave radiation (arrow indicates direction)
            \lceil Wm^{-2} \rceil
            directional longwave radiation (i denotes N, E, S, W, up, down)
L_i
            longwave radiation for sky pixels in thermal panorama [Wm<sup>-2</sup>]
L_{sky}
            longwave radiation for non-sky pixels in thermal panorama
L_{pixel}
            [Wm^{-2}]
            relative optical air mass
m_{RO}
N
            degree of cloudiness [octas]
PET
            physiologically equivalent temperature [°C]
R
            mean radiant flux density [Wm<sup>-2</sup>]
RH
            relative humidity [%]
T_a
            air temperature [°C]
T_L
            Linke turbidity factor (4.2)[-]
T_{ped}
            pedestrian surface temperature at street level [°C]
T_s
            surface temperature [°C]
T_{MRT}
            mean radiant temperature [°C]
UTCI
            Universal Thermal Climate Index
            wind velocity [ms<sup>-1</sup>]
V_p
            vapor pressure [hPa]
            altitude [m]
z
            albedo (0.15) [-]
α
            optical thickness
\delta_{RO}
            standard emissivity (0.95 [-]
ε
            emissivity of the human body (0.97) [-]
\varepsilon_{v}
            Sun's altitude (elevation) angle above the horizon [°]
η
φ
            solar zenith angle [°]
θ
            azimuth angle [°]
\xi_k
            absorption coefficient for shortwave radiation (0.7) [-]
            local atmospheric pressure [hPa]
ρ
            atmospheric pressure at sea level (1013) [hPa]
\rho_0
            Stefan-Boltzman constant (5.670367 \cdot 10^{-8}) [Wm<sup>-2</sup> K<sup>-4</sup>]
σ
```

## 1. Introduction

Land use and land cover change from urbanization coupled with climate change leads to urban overheating, i.e. thermal conditions in cities that are hazardous to people and associated urban systems (Nazarian et al., 2022). Heat has myriad negative impacts on human health (Gasparrini et al., 2015; Luber and McGeehin, 2008), comfort (Kuras et al., 2017; Middel et al., 2016), productivity (Dunne et al., 2013; Kjellstrom and Crowe, 2011), and performance (Alhadad et al., 2019; Kosaka et al., 2018). It also increases cooling energy use (Li et al., 2012), water use for irrigation (Jenerette et al., 2011), stresses urban infrastructure (Clark et al., 2019),

transmittance of direct solar radiation [-]

and negatively impacts the economy (Xia et al., 2018; Zander et al., 2015). Hotter weather is expected in the future (Russo et al., 2014), with more frequent and intense heat waves that may jeopardize the livability and sustainability of cities. Keeping people cool through targeted heat mitigation interventions is a priority of the 21st century (Broadbent et al., 2022; Jay et al., 2021).

While heat can be quantified using various temperature metrics, one of the most relevant metrics to assess human thermal exposure is the Mean Radiant Temperature ( $T_{MRT}$ ), as it provides an important summary assessment of the radiation exchange between the human body and the built environment (ISO, 1998; Johansson et al., 2014; Kántor and Unger, 2011; Middel et al., 2016).  $T_{MRT}$  is a synthetic parameter that quantifies the heat load on the human body through weighted omnidirectional shortwave and longwave radiation flux densities. Under hot, dry, clear-sky weather conditions,  $T_{MRT}$  is the main meteorological factor that drives spatial variation of human thermal comfort (Lin et al., 2010) and an important parameter in many thermal comfort indices that incorporate radiative exposure, such as the Physiological Equivalent Temperature (*PET*) (Höppe, 1999) and Universal Thermal Comfort Index (*UTCI*) (Blazejczyk et al., 2012; Fiala et al., 2012; Jendritzky et al., 2012).

 $T_{MRT}$  varies significantly in the built environment with reported differences of over 35 °C in the afternoon shade and sun (Middel et al., 2021). While spatial and temporal variation of  $T_{MRT}$  is mostly driven by shortwave radiation, lateral longwave radiation is the largest contributor to  $T_{MRT}$  in warm climates (Middel and Krayenhoff, 2019). Lindberg et al. (2014) showed that longwave fluxes become increasingly important in dense built environments with increased radiant fluxes from walls, highlighting the importance of vertical surface temperatures ( $T_s$ ) for human thermal exposure. Stewart et al. (2021) introduced the concept of pedestrian surface temperature ( $T_{ped}$ ), which is the weighted average of all surfaces surrounding a street-level pedestrian and is more relevant to human thermal exposure than horizontal  $T_s$  observed from above using satellite thermal imagery.

The built environment is a complex patchwork of differently oriented surface types with varying diurnal sun-exposure and radiative, thermal, roughness, and moisture characteristics, which leads to significant variations of  $T_s$  patches that contribute to  $T_{ped}$  in the urban canopy layer. Accurate  $T_s$  estimates are important for thermal exposure assessments, but spatially explicit  $T_s$  have not traditionally been observed in urban climate studies and are difficult to model without detailed 3-dimensional information on the composition and configuration of those  $T_s$  patches.

The emerging field of Urban Climate Informatics (Middel et al., 2022) offers novel sensing techniques and embraces more integrated and human-centric methods, including approaches to sense spatially resolved  $T_s$  in the urban canopy layer. For example, Aviv et al. (2021) used a rotating non-contacting infrared  $T_s$  sensor and LiDAR to create 3-dimensional  $T_s$  point clouds. Merchant et al. (2022) developed a camera system that records 360° shortwave and longwave panoramic images to fully resolve the spatial variation in shortwave and longwave radiant heat transfer in the outdoor environment.

We present an instrument setup to measure an approximation of  $T_{ped}$  in the form of thermal equirectangular 360° panoramas and introduce PanoMRT, an open source human thermal exposure and comfort model that calculates  $T_{MRT}$ , PET, and UTC from standard meteorological information and detailed  $T_s$  observations. Model results are validated using the mobile 6-directional instrument setup MaRTy (Middel and Krayenhoff, 2019) and compared to RayMan  $T_{MRT}$  calculations without  $T_s$  forcing to demonstrate the importance of spatially explicit, human-centric  $T_s$  data for human thermal exposure and comfort modeling.

## 2. Methods

PanoMRT is a Python-based software that calculates  $T_{MRT}$  from observed longwave radiation fluxes and modeled shortwave radiation fluxes simulating a 6-directional net radiometer setup for integral radiation measurements. To model  $T_{MRT}$  for a given location, time, and day, PanoMRT

requires a 360° equirectangular thermal panorama of the location and standard weather information (Fig. 1). The thermal panorama is projected into six fisheye images to calculate integral longwave radiation fluxes from pixel surface temperatures  $T_s$  and determine the sky view factor ( $f_{SVF}$ ) of the location. The sun position (i.e., solar azimuth  $\theta$  and zenith  $\phi$ ) is calculated from the latitude, date, and time of panorama acquisition. Standard weather data (air temperature  $T_a$ , relative humidity RH, and wind speed  $\nu$ ) can be input from in-situ observations or automatically retrieved from the closest airport via the OpenWeather Application Programming Interface (API). 6-directional contributions of direct and diffuse shortwave radiation are then estimated from atmospheric conditions. Additional input parameters capturing characteristics of the pedestrian are used to calculate the thermal indices PET and UTCI.

## 2.1. Mean radiant temperature modeling

 $T_{MRT}$  is defined as the "uniform temperature of an imaginary enclosure in which the radiant heat transfer from the human body equals the radiant heat transfer in the actual non-uniform enclosure" (ISO, 1998). It is calculated from the mean radiant flux density R using the Stefan-Boltzmann law:

$$T_{MRT} = \sqrt[4]{R/\varepsilon_p \sigma - 273.15} \left[ {^{\circ}C} \right]$$
 (1)

R summarizes the long-( $L_i$ ) and shortwave ( $K_i$ ) radiation fluxes the human body is exposed to from six directions (i) (VDI, 1994) and can be observed using a 6-directional setup or integral radiation measurements (Höppe, 1992):

$$R = \xi_k \sum_{i=1}^6 K_i F_i + \varepsilon_p \sum_{i=1}^6 L_i F_i \tag{2}$$

 $F_i$  are angular weighting factors for a standing person and set to 0.22 for lateral radiation fluxes and 0.06 for upwards and downwards directed fluxes to approximate the elongated body shape (Fanger, 1972).  $\xi_k$  is an absorption coefficient for shortwave radiation (0.7), and  $\varepsilon_p$  is the emissivity of the human body (0.97) (VDI, 1994).

While PanoMRT estimates the longwave components of R from observed, pixel-based  $T_s$  in thermal panoramas, it uses a hybrid radiation flux density modeling approach that draws from existing  $T_{MRT}$  models to calculate diffuse and global shortwave radiation and directional shortwave radiation (Lindberg et al., 2008; Lindberg and Grimmond, 2011).

# 2.1.1. Shortwave radiation

The shortwave radiation  $K_i$  for each of the six directions depends on the sun position and has a direct (I) and diffuse (D) component. The direct shortwave radiation I on a horizontal surface can be calculated as the portion of extraterrestrial solar radiation  $\bar{I}_0$  that travels through the atmosphere (VDI, 1994):

$$I_0 = \overline{I}_0 \cdot (1 + 0.03344 \cdot \cos((DOY \cdot 0.9856 - 2.72) \cdot \pi/180^\circ))$$
 (3)

 $I_0$  is calculated using the solar constant  $\bar{I}_0 = 1367 \text{ Wm}^{-2}$  and day of year (*DOY*) to determine the length of the path (the air mass) the radiation must travel. To consider atmospheric absorption and scattering of the incoming solar radiation, I can then be formulated as (Jendritzky, 1990):

$$I = I_0 \cdot \sin \eta e^{(-T_L \cdot \delta_{RO} \cdot m_{RO} \cdot \rho/\rho_0)} \cdot (1 - N/8)$$
(4)

where  $T_L$  is the Linke Turbidity factor (denotes the transparency of the cloudless atmosphere);  $\rho/\rho_0$  is the pressure correction for reducing the optical thickness of the standard atmosphere at sea level (1013.25 hPa) to the current atmospheric pressure:

$$\rho = 101325 \cdot \left(1 - 2.25577 \cdot 10^{-5} \cdot \mathbf{z}\right)^{5.25588} \tag{5}$$

N is degree of cloudiness in octas;  $\delta_{RO}$  is the optical thickness (Kasten, 1980):

$$\delta_{RO} = 1/(0.9m_{RO} + 0.94) \tag{6}$$

 $m_{RO}$  is the relative optical air mass for a given sun elevation angle  $\eta$  (Kasten and Young, 1989):

$$m_{RO} = 1/\left(\sin\eta + 0.50572 \cdot (\eta + 6.07995^{\circ})^{-1.6364}\right)$$
 (7)

Eq. (7) only holds for  $\eta > 5^{\circ}$ ; for lower sun elevation angles,  $\delta_{RO}$  has to be retrieved from a look-up table (Matzarakis et al., 2010).

The diffuse shortwave radiation D is composed of an isotropic ( $D_{iso}$ ) and anisotropic ( $D_{aniso}$ ) component and interpolated linearly between cloudless (N=0) and overcast (N=8) weather conditions (Matzarakis et al., 2010):

$$D = (D_{iso} + D_{aniso}) \cdot (1 - N/8) + 0.28G_0 \cdot f_{SVF} \cdot N/8$$
(8)

The isotropic component  $D_{iso}$  depends on the sky view factor  $f_{SVF}$ , the direct shortwave radiation I on a horizontal surface, the global radiation  $G_0$  for  $f_{SVF}=1$  and cloudless conditions, and the transmittance of direct solar radiation  $\tau$ :

$$D_{iso} = (G_0 - I(N = 0)) \cdot (1 - \tau) \cdot f_{SVF}$$
(9)

$$G_0 = 0.84 \cdot I_0 \cdot \cos \phi \cdot e^{\left(-0.027 \frac{\rho}{\rho_0} \cdot \frac{T_L}{\cosh}\right)} \tag{10}$$

$$\tau = I(N=0)/(I_0 \cos \phi) \tag{11}$$

For shaded locations, the anisotropic component  $D_{aniso}$  is omitted; for sun-exposed locations, it is calculated as follows:

$$D_{aniso} = (G_0 - I(N = 0)) \cdot \tau \tag{12}$$

The sky view factor  $f_{SVF}$  is calculated from individual thermal panoramas assuming that all pixels with  $T_S < 4$  ° C are sky pixels to distinguish them from urban surface pixels—a threshold that should be refined for other

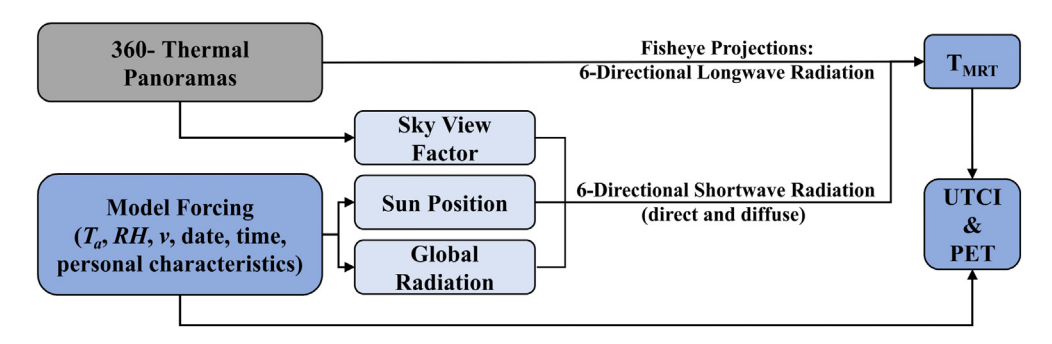


**Fig. 1.** *PanoMRT* model workflow including input (360° equirectangular thermal panorama, standard weather information, latitude/longitude, date, time, personal characteristics) and output (*T<sub>MRT</sub>, UTCI, PET*).

geographic locations and weather conditions. The panoramas are projected into hemispherical views, and each thermal fisheye is partitioned into n annular rings (n=32) to calculate  $f_{SVF}$  by summing up the contribution of non-sky pixels in each ring:

$$f_{\mathit{SVF}} = \frac{\pi}{2n} \Sigma_{j=1}^{n} \, \sin\!\left(\!\frac{\pi(2j-1)}{2n}\!\right) \! \left(\!\frac{p_{j}}{t_{j}}\!\right) \eqno(13)$$

where  $p_j/t_j$  is the ratio between the number of sky pixels to the total number of pixels in ring j (Middel et al., 2017, 2018; Steyn, 1980). The hemispherical fisheye is further used to determine if a position is shaded or sun-exposed at any given time by determining the sun position in the fisheye and calculating the percent sky vs. non-sky pixels in a 3-by-3 pixel neighborhood.

To calculate the total shortwave radiation K including direct and diffuse radiation, we consider each of the six directions separately and use a simplified formulation by Lindberg and Grimmond (2011). The incoming shortwave radiation  $K_{\downarrow}$  from the upper hemisphere is a function of the direct solar radiation on the plane normal to the direction of incidence  $I' = I/\sin\eta$  and the diffuse radiation D (ignoring reflections from surfaces in the surroundings):

$$K_{\downarrow} = I' \cdot \sin \eta + D = I + D \tag{14}$$

The outgoing shortwave radiation  $K_{\uparrow}$  is calculated as a fraction of the incoming shortwave, assuming that all surrounding surfaces are sunexposed and have an average albedo of  $\alpha=0.20$ :

$$K_{\uparrow} = K_{\downarrow} \cdot \alpha \tag{15}$$

The lateral reflected shortwave radiation is calculated as  $K_{\rightarrow} = K_{\downarrow} \cdot \alpha \cdot 0.5$  for sun-exposed locations, ignoring reflections from vertical features and

assuming that all ground surfaces in the surrounding are sun-exposed (view factor of the ground is 0.5 in lateral fisheye views). The incoming lateral shortwave radiation depends on the cardinal direction (N, E, S, W) and will only be calculated for the two directions in which the sun is visible in the lateral fisheye projection, i.e.,

$$N: \theta \ge 270^{\circ} \qquad K_{\rightarrow} = I' \cdot \cos \eta \cdot \sin(\theta - 270^{\circ}) + D \qquad (16)$$

$$N: \theta < 90^{\circ} \qquad K_{\rightarrow} = I' \cdot \cos \eta \cdot \sin(\theta + 90^{\circ}) + D \qquad (17)$$

$$E: 0^{\circ} \le \theta < 180^{\circ}$$
  $K_{\rightarrow} = I' \cdot \cos \eta \cdot \sin \theta + D$  (18)

$$S: 90^{\circ} \le \theta < 270^{\circ} \qquad K_{\rightarrow} = I' \cdot \cos \eta \cdot \sin(\theta - 90^{\circ}) + D \tag{19}$$

W: 
$$180^{\circ} \le \theta < 360^{\circ}$$
  $K_{\rightarrow} = I' \cdot \cos \eta \cdot \sin(\theta - 180^{\circ}) + D$  (20)

If  $\theta$  falls outside the given range or the location is shaded, I' = 0.

## 2.1.2. Longwave radiation

Longwave radiation fluxes  $L_i$  in six directions are calculated from equirectangular thermal panoramas. To mirror a 6-directional net radiometer setup, the panoramas are projected into six fisheye views (Fig. 2) by relating pixels  $(x_p, y_p)$  of a WxH sized panorama to pixels  $(x_f, y_f)$  of a fisheye view with center pixels  $(C_x, C_y)$  using the following transformation:

$$x_{p} = \begin{cases} \left( \pi/2 + \tan^{-1} \left[ \left( y_{f} - C_{y} \right) / (x_{f} - C_{x}) \right] \right) \cdot W / 2\pi, x_{f} < C_{x} \\ \left( 3\pi/2 + \tan^{-1} \left[ \left( y_{f} - C_{y} \right) / (x_{f} - C_{x}) \right] \right) \cdot W / 2\pi, x_{f} > C_{x} \end{cases}$$
(21)

$$y_p = H \cdot W/2\pi \left( \sqrt{(x_f - C_x)^2 + (y_f - C_y)^2} \right)$$
 (22)

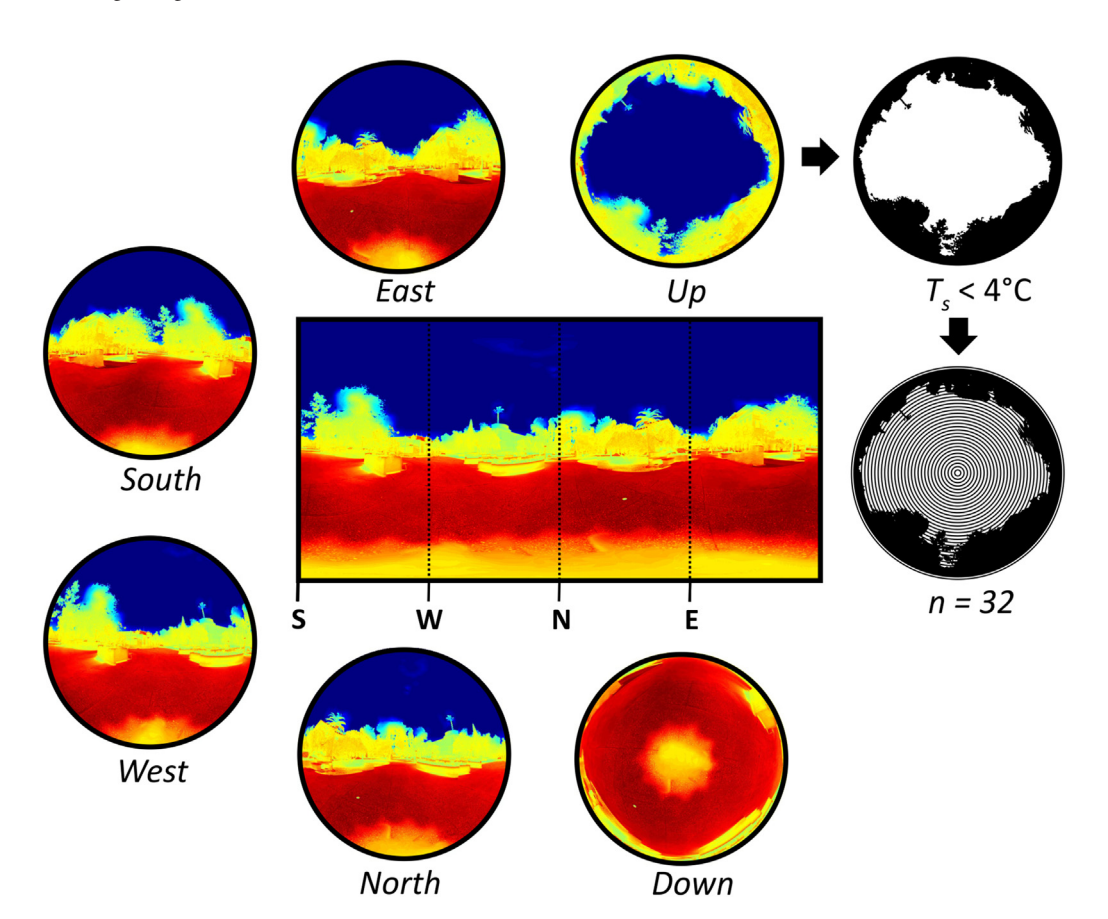


Fig. 2. Thermal panorama projection into 6-directional fisheye views; sky detection in thermal fisheyes using a threshold of  $T_S < 4$  °C; and sky view factor ( $f_{SVF}$ ) calculation using 32 annulus rings.

For each directional thermal fisheye,  $T_s$  of non-sky pixels is converted to a longwave radiation flux assuming a standard emissivity of  $\varepsilon=0.95$  and atmospheric radiation A as follows:

$$L_{pixel} = \varepsilon \sigma (T_s + 273.15)^4 + (1 - \varepsilon) \cdot A$$
 (23)

$$A = \sigma \cdot (T_a + 273.15)^4 \cdot (0.82 - 0.25 \cdot 10^{-0.0945 \cdot V_p}) \cdot (1 + 0.21 \cdot (N/8)^{2.5})$$
(24)

Longwave radiation for sky pixels is estimated from  $T_a$  and sky emissivity  $\varepsilon_{sky_2}$  which is a function of vapor pressure  $V_p$  and  $T_a$  (Lindberg et al., 2008):

$$L_{\text{sky}} = \varepsilon_{\text{sky}} \sigma (T_a + 273.15)^4 \tag{25}$$

$$\varepsilon_{\text{sky}} = 1 - \left(1 + 46.5 \frac{V_p}{T_a + 273.15}\right) \cdot e^{\left(-\left(1.2 + 3.0 \cdot 46.5 \frac{V_p}{T_a + 273.15}\right)^{0.5}\right)}$$
(26)

Finally,  $L_i$  is calculated for each directional thermal fisheye by summarizing average longwave radiation values over 32 annulus rings (analogous to the  $f_{SVF}$  calculation) and inserted in Eq. (2) along with the directional shortwave radiation fluxes  $K_i$  (Eqs. (14)–(20)) to yield the mean radiant flux density R and subsequently  $T_{MRT}$ .

#### 2.2. Thermal comfort index calculations

Thermal comfort is a complex function of environmental factors determining thermal exposure and physiological, psychological, and behavioral factors (Chen and Ng, 2012; Johansson et al., 2014; Middel et al., 2016; Nikolopoulou and Lykoudis, 2006). Numerous thermal comfort indices have been developed to integrate environmental and personal factors into an experienced temperature value (Potchter et al., 2018). The current implementation of *PanoMRT* calculates *PET* (Höppe, 1999) and *UTCI* (Blazejczyk et al., 2012; Fiala et al., 2012; Jendritzky et al., 2012) based on user-configured personal characteristics (age, gender, height, weight), metabolic rate, and clothing insulation.

## 3. Model validation

PanoMRT was validated through in-situ observations of humanbiometeorological data at the time of thermal panorama acquisition. Model performance was assessed using standard model statistics such as the Root Mean Square Error (RMSE), Mean Bias Error (MBE), and the index of agreement (d) (Willmott, 1982). In addition, PanoMRT results were compared to RayMan (Matzarakis et al., 2010) simulations to assess the benefit of spatially explicit  $T_s$  observations for location-based  $T_{MRT}$ modeling. For this comparison, RayMan was run with hemispherical black and white images generated from the thermal panoramas (assuming a threshold of 4 °C for sky pixels) and the same meteorological forcing as PanoMRT (observed  $T_a$  and RH but not  $T_s$ ). Lastly, PET and UTCI were calculated from human-biometeorological observations ( $T_a$ ,  $T_{MRT}$ , RH,  $\nu$ ) and default parameters for personal characteristics for PET (35-year old male, 1.75 m, 75 kg, clothing insulation 0.5 clo, metabolic rate  $80 \text{Wm}^{-2}$ ) for comparison to PanoMRT and RayMan results to determine the impact of spatially explicit  $T_s$  on thermal index calculations.

## 3.1. Study site

*PanoMRT* was developed, tested, and validated in hot and dry Tempe, Arizona, USA. Tempe is situated in the East Valley of the Phoenix metropolitan area, a region in the Sonoran Desert of the U.S. Southwest with low annual rainfall (237 mm) and low relative humidity (Köppen Climate Classification subtype *Bwh*). With an average of 300 clear, sunny days per year, air temperature peaks at or above 32 °C for an average of 175 days, and maximum air temperatures frequently surpass 43 °C in June. To test and validate *PanoMRT*, we chose 18 locations on Arizona State University's

Tempe campus that are within walking distance from each other to allow for transect observations (Fig. 3). The campus is a 2.6-km<sup>2</sup> area of interconnected pedestrian malls and can be considered an open midrise local climate zone (Stewart and Oke, 2012). We selected diverse sites with respect to ground cover (asphalt, concrete, grass), sky view factor ( $f_{SVF}$ ), and shading (trees, building tunnel, engineered shade canopies, fully exposed). In addition, we conducted field observations on the Phoenix Zoo main parking lot, which is located 5 km north of campus and has minimal horizon limitation ( $f_{SVF} = 0.98$ ).

## 3.2. Thermal panorama retrieval and $T_{MRT}$ observations

Thermal panoramas were acquired on campus along with in-situ observations of human-biometeorological data on three hot, dry, clear summer days in summer 2020: May 27, May 28, and June 16. Observational walking transects were conducted every 3 h from 6:00 h to 20:00 h local time covering five to six locations per day. The Phoenix Zoo parking lot location was monitored hourly on June 3, 2020 from 7:00 h to 17:00 h.

A FLIR Duo Pro R Dual-Sensor 4K Thermal Camera ( $640 \times 512$  pixels,  $45^{\circ}$  horizontal field of view) was attached to a Gigapanos rotational arm on a tripod to automatically capture a matrix of  $8 \times 10$  visual and thermal images with 25 % overlap at each location (Fig. 4b). A complete  $360^{\circ}$  scan took about 5 min. In post-processing, the sets of visual images were arranged in a grid and stitched into an equirectangular panorama using the stitching software PTGUI. The stitching parameters then served as a template for creating the corresponding thermal panoramas (Fig. 5).

 $T_{MRT}$  was observed at each location using the mobile weather station MaRTy (Middel et al., 2021; Middel and Krayenhoff, 2019). MaRTy is a human-biometeorological instrument platform that records 6-directional radiation flux densities ( $L_i$  and  $K_i$ ),  $T_a$ , horizontal wind speed ( $\nu$ ), and relative humidity (RH) at 2 s intervals (Fig. 4a). The platform was placed in the center of the panorama tripod location immediately after each thermal scan to collect human-biometeorological data for 1–2 min. The first 15 records at each location were removed to account for the response time of the  $T_a/RH$  probe (sensor time constant 22 s, 63 % step change) and minimize the impact of sensor lag (Häb et al., 2015); the remaining records were averaged for each location and time to provide localized forcing data for the PanoMRT validation ( $T_a$ , RH,  $\nu$ ) and  $T_{MRT}$  ground truth.

#### 3.3. Results

# 3.3.1. Meteorological conditions and in-situ observations

Meteorological conditions were similar across field work days with minimum  $T_a$  between 24 °C and 31 °C, maximum  $T_a$  between 41 °C and 43 °C, and clear, sunny skies. RH ranged between 21 % and 25 % at 6:00 h and below 10 % during the afternoon hours. Wind speed was generally low (<1.0 m s  $^{-1}$  on average across all observations) with peak gusts of up to 4.3 m s  $^{-1}$ .

 $T_{MRT}$  varied considerably across locations and times of day, especially between sun-exposed and shaded sites (Fig. 6).  $T_{MRT}$  peaked in the afternoon (between 15:00 h and 16:00 h) at open locations with high  $f_{SVF}$ , such as the sun-exposed parking lot location 10 ( $f_{SVF}=0.84$ ) with 72.3 °C and the concrete path intersection 12 ( $f_{SVF}=0.81$ ) with 71.0 °C. In contrast,  $T_{MRT}$  was close to  $T_a$  during the day under large, dense shade trees (locations 4, 16, and 2) and below  $T_a$  inside a tunnel through a parking garage (location 8). After sunset,  $T_{MRT}$  was highest in a narrow east-west canyon enclosed by concrete walls (location 6, 35.6 °C), under a metal shade structure (location 1, 35.6 °C), and inside the tunnel (location 8, 36.9 °C). Coolest  $T_{MRT}$  was recorded over grass after sunset (location 11,  $f_{SVF}=0.93$ , 22.9 °C).

Surfaces showed the greatest variability in temperature across surface types, sun exposure level, and times of day. Irrigated grass exhibited the lowest  $T_s$  at 6:00 h with 19.8 °C (location 3) and 19.2 °C (location 11) and did not exceed  $T_a$  throughout the day. The hottest ground  $T_s$  in excess of 60 °C was recorded midday over a concrete path (location 12), an asphalt road (location 9), and the Phoenix Zoo asphalt parking lot (location 10).



Fig. 3. Equirectangular panoramas of 18 observation sites on Arizona State University's Tempe campus and one site on the Phoenix Zoo parking lot (upper left panorama, location outside map 5 km north of campus). For site metadata (fisheye photos, exposure, ground cover, sky view factor) see Supp. Table 1.

The thermal panoramas illustrate the  $T_s$  distribution of surfaces in the 360° surroundings of each location (Fig. 7).

## 3.3.2. PanoMRT and RayMan model performance

*PanoMRT* performs well overall (Supp. Table 3) with a Root Mean Square Error (*RMSE*) of 4.1 °C for all observations (N=145), which meets the accuracy requirement of  $\pm 5$  °C set in the ISO 7726 standard

(ISO, 1998) for heat and cold stress studies. The model exhibits an unsystematic *RMSE* of  $4.5\,^{\circ}C$  and a systematic *RMSE* of  $0.7\,^{\circ}C$ , indicating that model parameters are well-specified and the majority of the error results from processes or model-observation differences beyond the scope of the current model. This includes errors associated with observation procedures and instrumentation setup: human-biometeorological observations and thermal panoramas were not taken at the same time but successively, and



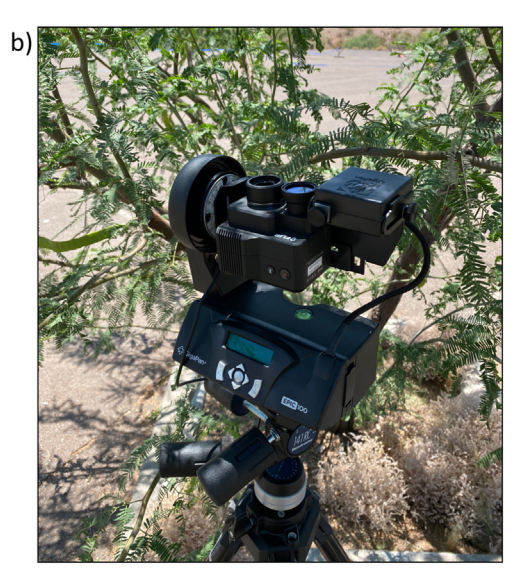


Fig. 4. a) Mobile human-biometeorological instrument platform MaRTy (Middel et al., 2021; Middel and Krayenhoff, 2019); b) FLIR Duo Pro R Dual-Sensor 4K Thermal Camera on a Gigapanos rotational arm. For instrument specifications see Supp. Table 2.

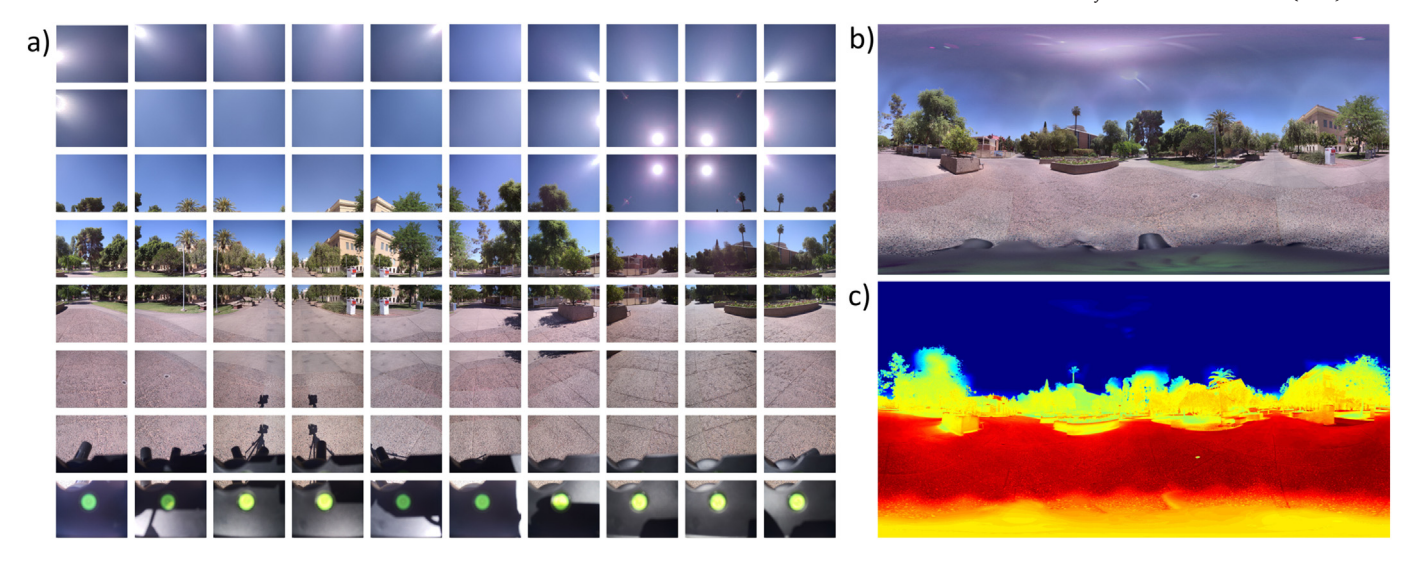


Fig. 5. a) Matrix of 8 × 10 overlapping photos from panorama scan at location 12; b) stitched visual panorama; c) corresponding stitched thermal panorama.

*MaRTy*'s net radiometers are subject to varying spatial exposure, because they are 0.6–1.0 m apart. The Mean Bias Error (*MBE*) captures the average bias in the prediction and is negative (-1.9 °C), meaning that *PanoMRT* tends to underestimate  $T_{MRT}$ . The slope of the regression line (Supp. Fig. 1) supports this observation. The Mean Absolute Error (*MAE*), i.e. the sum of absolute errors divided by the sample size, is 3.2 °C, and the index of agreement (d), i.e. a standardized measure of the degree of model prediction error, shows excellent agreement with d=0.98.

PanoMRT performance varies by time of day (6:00 h, 9:00 h, 12:00 h, 15:00 h, 18:00 h, 20:00 h), exposure (sun/shade), and shade type (tree/ engineered) (Fig. 8). The lowest RMSE (3.3 °C) is observed at 20:00 h when incoming shortwave radiation is zero and the model solely relies on the measured thermal panorama input. At this time of day, errors can be attributed to an assumed fixed emissivity (0.95) for the thermal images, the assumption that reflected longwave from surfaces originates from the sky only, inaccuracies in the sky detection at the transition between the built environment and sky, and the tripod surface temperature, which is in the field of view of the camera and obstructs parts of the ground. In addition, the model tends to underestimate  $T_s$  for sky pixels and therefore L for open sites with a large  $f_{SVF}$  (overall RMSE = 3.8 °C, MAE 3.0 °C, d = 0.93). Model results after sunrise (6:00 h) exhibit the highest RMSE (5.0 °C) with a negative MBE (-2.3 °C). PanoMRT underestimates incoming solar radiation at low sun angles, and meteorological conditions change quickly after sunrise, which introduces differences in MaRTy and thermography observations that impact model validation and add to unsystematic errors. The model performs equally well for engineered shade (RMSE = 4.2 °C) and tree shade (RMSE = 4.1 °C) due to available surface temperature observations for both shade types from thermal panoramas. Systematic errors are low for all times of day, exposures, and shade types. The largest RMSEs is observed at noon with 3.1 °C, otherwise RMSEs ranges between 0.7 °C and 1.6 °C.

PanoMRT performance also varies by location due to heterogeneous urban forms. A majority of sites (120 of 145 observations across space and time) exhibit a <5 °C difference between modeled and observed  $T_{MRT}$ , and more than half (75) of the modeling results are within 3 °C of the MaRTy observations. Two sites show large discrepancies in the morning:  $T_{MRT}$  at location 18 (under a Palo Verde tree,  $f_{SVF}=0.17$ ) is overestimated by 11.2 °C during the 9:00 h transect, and  $T_{MRT}$  at location 15 (sun-exposed concrete crossing,  $f_{SVF}=0.87$ ) is overestimated by 11.2 °C during the 6:00 h transect. Both observations are subject to measurement errors as one of MaRTy's net radiometers was inadvertently shaded. In contrast, PanoMRT significantly underestimates  $T_{MRT}$  for locations 11 (lawn next to Arizona State University's Hayden library,  $f_{SVF}=0.85$ ) at 18:00 h, 1 (metal shade structure,  $f_{SVF}=0.10$ ) at 16:00 h, and

17 (photovoltaic shade structure,  $f_{SVF}=0.04$ ) at 12:00 h. The difference in modeled and observed  $T_{MRT}$  of  $-10.8\,^{\circ}\mathrm{C}$  for location 11 is due to the low sun elevation angle that leads to underestimated incoming shortwave radiation in the model.  $T_{MRT}$  estimation errors under engineered shade result from inadvertent sun exposure of a net radiometer due to the offcenter placement of the sensors. Overall, the most challenging location for PanoMRT to estimate  $T_{MRT}$  is 19 ( $f_{SVF}=0.37$ ), which is a plaza surrounded by tall palm trees. The model is unable to handle semi-shade or dappled shade and underestimates  $T_{MRT}$  by  $-5.6\,^{\circ}\mathrm{C}$  to  $-7.6\,^{\circ}\mathrm{C}$  when the sun is not visible in the upper hemisphere (obstructed by palm leaves, shaded) and overestimates  $T_{MRT}$  by  $5.8\,^{\circ}\mathrm{C}$  for the sun-exposed case at 12:00 h.

*RayMan* has an overall *RMSE* of 9.0 °C (Supp. Table 3) with an unsystematic *RMSE* of 7.8 °C (mostly due to observation procedures and instrumentation setup) and a systematic *RMSE* of 4.4 °C. The *MBE* for all observations (N=145) is positive, indicating that RayMan tends to overestimate  $T_{MRT}$ . The *MAE* is 7 °C, and the index of agreement shows good overall model performance (d=0.89).

*RayMan* performance varies significantly by time of day, exposure, and shade type (Fig. 8). The lowest *RMSE* is observed after sunset (3.2 °C). Model results at 12:00 h and 15:00 h exhibit the highest *RMSE* (11.0 °C and 11.4 °C), the highest *MAE* (8.5 °C and 10.6 °C), and the lowest *d* (0.42 and 0.51). During mid-day, *I* and  $T_s$  peak, therefore modeling errors in emitted longwave radiation are expected to be largest. With respect to exposure, the *MBE* shows that *RayMan* overestimates shaded locations and underestimates sun-exposed locations. In the shade, the *RMSE* is 11.8 °C for trees and 9.2 °C for engineered shade, respectively, due to overestimation of surrounding  $T_s$ . In the sun, the *RMSE* amounts to 8.2 °C. The absence of reflected shortwave radiation in the model is likely a contributing factor to underestimated  $T_{MRT}$  values in sun-exposed locations.

RayMan performance varies significantly by location. Simulations are most accurate for open sites with high  $f_{SVF}$ . Half of the modeling results are within 5 °C of  $T_{MRT}$  observations, while only 46 model runs yield  $T_{MRT}$  results within 3 °C of MaRTy observations. Locations 8 (tunnel,  $f_{SVF}=0.00$ ), 7 (dense tree canopy cover,  $f_{SVF}=0.02$ ), 2 (dense tree canopy cover,  $f_{SVF}=0.02$ ), and 4 (medium dense tree canopy cover,  $f_{SVF}=0.32$ ) exhibit the largest  $T_{MRT}$  error of up to -24.9 °C, -19.3 °C, -18.1 °C, and -17.2 °C respectively, during the 12:00 h transect.  $T_{MRT}$  is overestimated at all times at the four locations due to a modeling error of shaded  $T_s$  of up to 8.8 °C, which translates into overestimated longwave emission.

In contrast, *RayMan* underestimates  $T_{MRT}$  by up to -17 °C for open locations 13 (lawn next to Arizona State University's Old Maine,  $f_{SVF}=0.84$ ) and 12 (sun-exposed concrete crossing,  $f_{SVF}=0.87$ ) at low sun angles

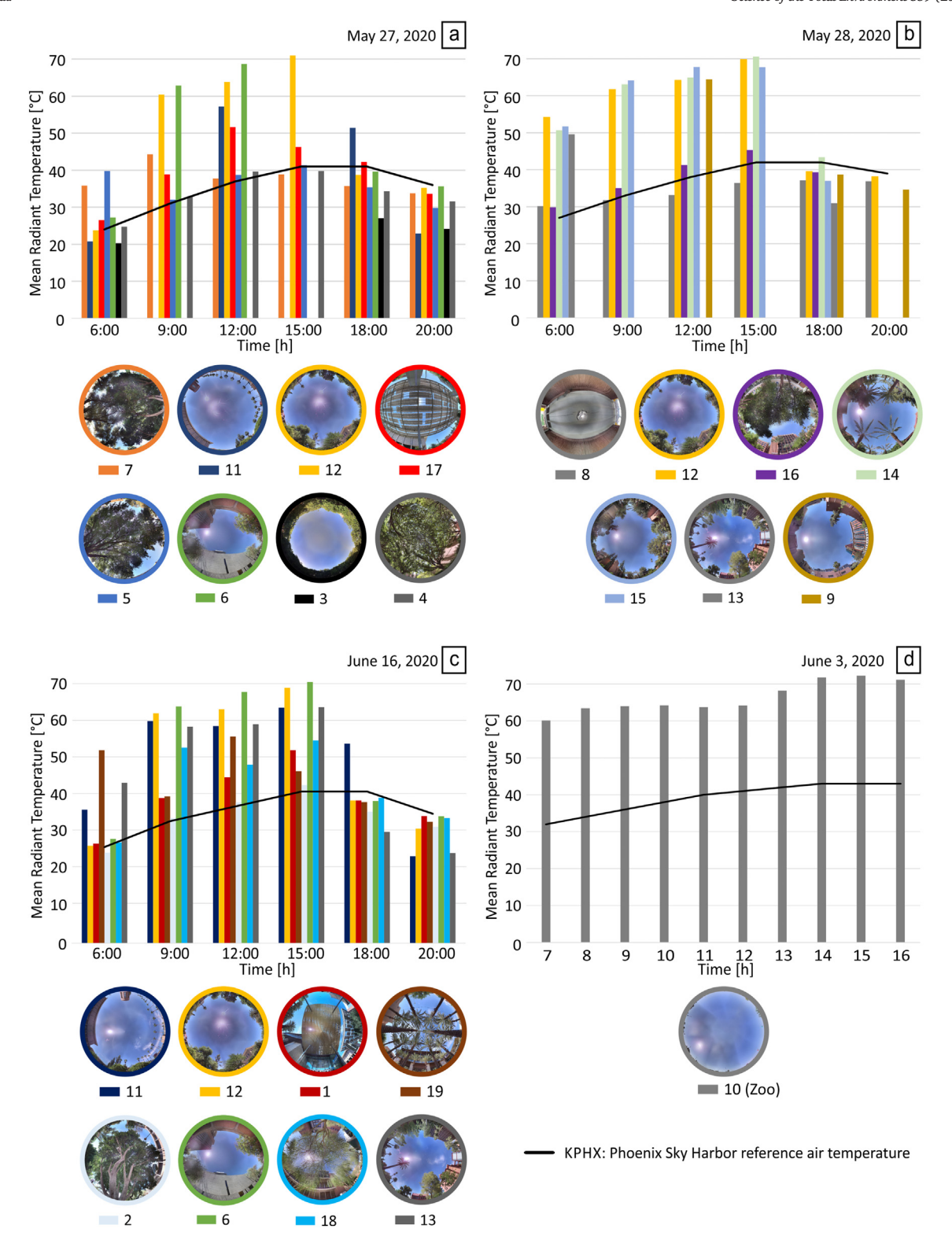


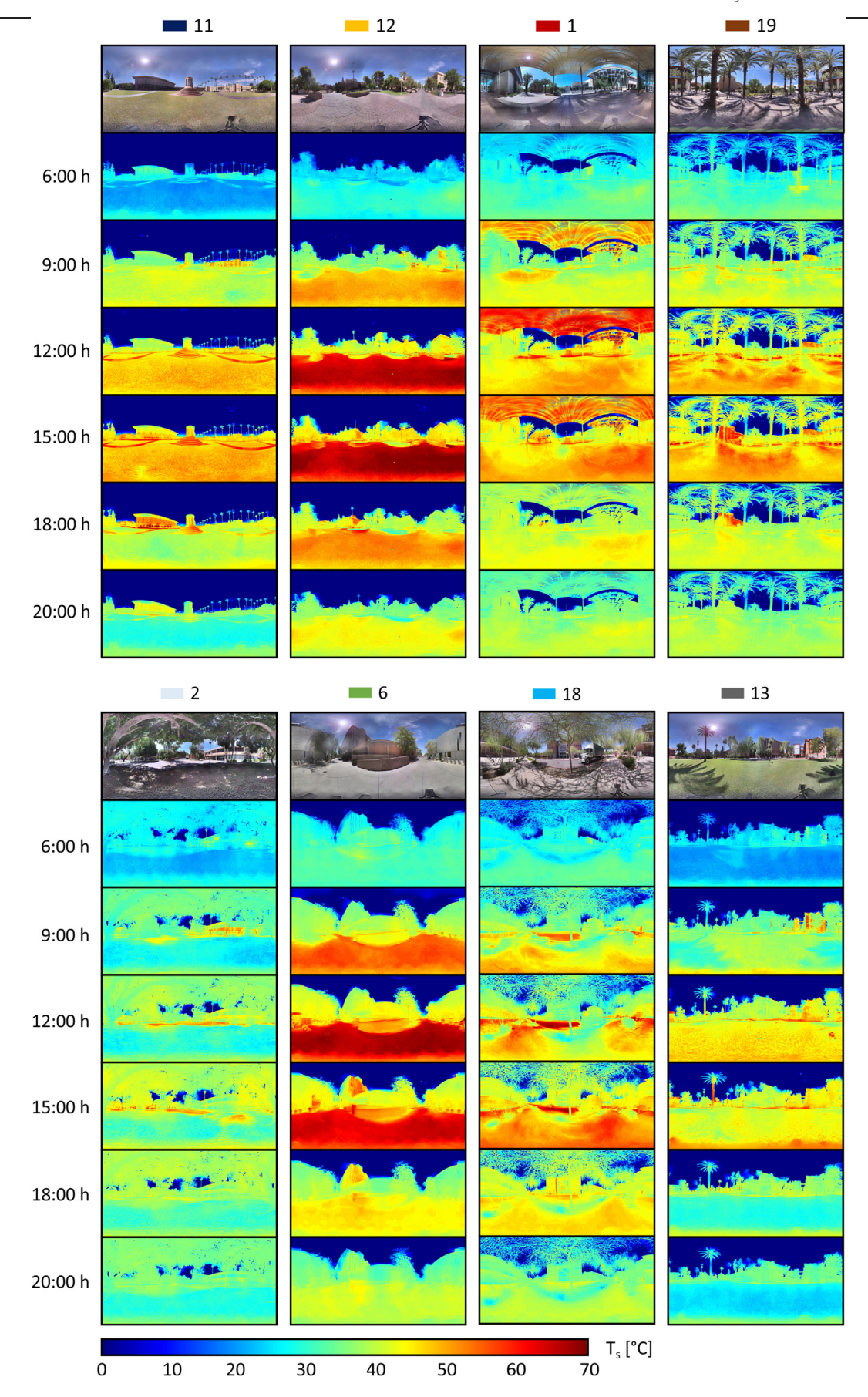
Fig. 6. In-situ mean radiant temperature observations with MaRTy for all field work days and locations: a) May 27, 2020; b) May 28, 2020; c) June 16, 2020; d) June 3, 2020.

during the 6:00 h transect. Some of these errors are due to inaccuracies in the fisheye photo where the pixel of the calculated sun position is black (i.e. the location is shaded) but the neighboring pixels are white, and the observations are actually sun-exposed (or vice versa, RayMan models sun-exposure for a shaded location). Analogous to PanoMRT, RayMan struggled to model the semi-shade of location 19 (plaza with tall palm trees,  $f_{SVF} = 0.37$ ), and measurement errors due to accidental sun or shade exposure of

one of MaRTy's net radiometers led to inadvertent differences in modeled and observed  $T_{MRT}$  for locations 18, 15, 17, and 1.

## 3.3.3. Mean radiant temperature error propagation into thermal indices

Since PET and UTCI are driven by  $T_{MRT}$ , modeling errors related to radiative heat fluxes propagate into PET and UTCI outcomes. Here, temperature, humidity, and wind speed are provided by the MaRTy



 $\textbf{Fig. 7.} \ \, \textbf{Thermal panoramas for all locations observed on June 16, 2020: after sunrise (6:00 \, h), mid-morning (9:00 \, h), midday (12:00 \, h), midday (12:0$ 

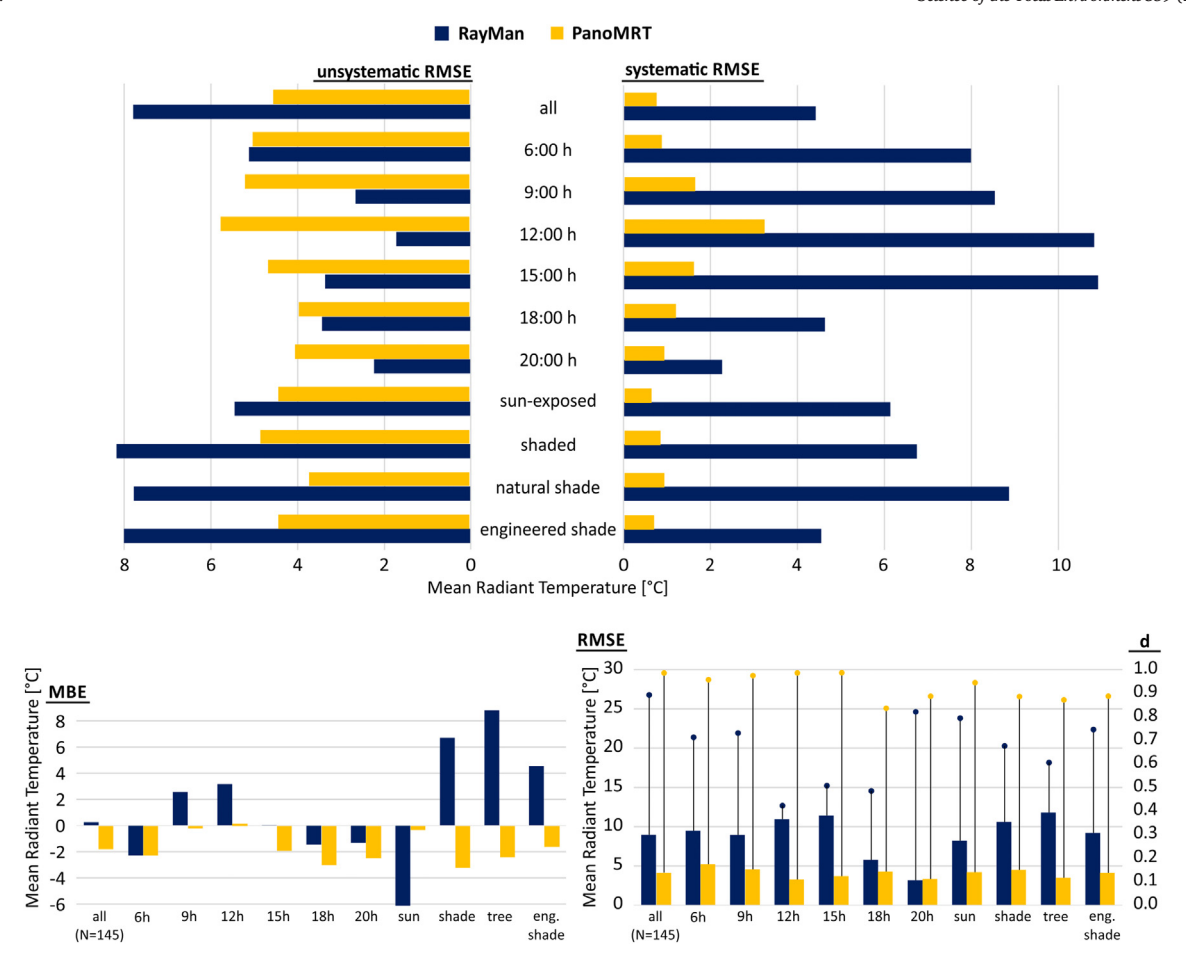


**Fig. 8.** Model performance statistics for *PanoMRT* and *RayMan* including Root Mean Square Error (*RMSE*), unsystematic *RMSE* (*RMSEu*), systematic *RMSE* (*RMSEs*), index of agreement (*d*), and Mean Bias Error (*MBE*). R<sup>2</sup> values are illustrated in Suppl. Fig. 1–3. Violin plots of *PanoMRT* model errors are shown in Suppl. Fig. 4. Performance statistics are summarized in suppl. Table 3.

biometeorological station, and therefore all errors in *PET* and *UTCI* derive from  $T_{MRT}$  modeling. PanoMRT results for PET yield an overall RMSE of 2.6 °C with an MAE of 2.2 °C, MBE of -1.53 (model tends to underestimate PET), and d of 0.97. Reference RayMan simulations without  $T_s$  forcing have an RMSE of 6.4 °C with an MAE of 5.3 °C, MBE of 4.80 (model tends to overestimate PET), and d of 0.85. Concurrent with  $T_{MRT}$  estimates, model results for PET meet the accuracy requirement of  $\pm$ 5 °C set in the ISO 7726 standard for heat and cold stress studies when spatially explicit  $T_s$  are used as model input. UTCI is less sensitive to  $T_{MRT}$  and  $T_s$  of the built environment. PanoMRT models UTCI with an RMSE of 1.22 °C and RayMan with an RMSE of 2.31 °C.

## 4. Discussion

Since PanoMRT and RayMan have similar procedures to calculate incoming shortwave radiation, forcing both models with MaRTy observed human-biometeorological data and comparing results allows to quantify the benefit of using spatially explicit, human-centric, 3-dimensional  $T_s$  ( $T_{ped}$ ) for  $T_{MRT}$  modeling. RayMan exhibits larger errors than PanoMRT for all times, exposures, and shade types except at 20:00 h when RMSE is similar (3.2 °C and 3.3 °C). Overall, thermal panoramas reduce RMSE from 9.0 °C to 4.1 °C, which meets the accuracy requirement of  $\pm$  5 °C set in the ISO 7726 standard. The biggest model performance boost is observed at 12:00 h when  $T_s$  are highest. RMSE improves from 11.0 °C to 4.0 °C while d increases from 0.42 to 0.97. Previous studies confirm that RayMan overestimates  $T_s$  for enclosed sites, especially during the summer, which results in a large positive MBE for shaded sites with low  $f_{SVF}$  (Colter et al., 2019; Crank et al., 2020; Gál and Kántor, 2020; Krüger et al., 2014; Lee and

Mayer, 2016). While sun exposure is the main driver of variability in  $T_{MRT}$  under clear sky conditions (Lee et al., 2014; Lindberg et al., 2016), longwave fluxes gain importance in denser built environments (Lindberg et al., 2014). Middel and Krayenhoff (2019) found that lateral components of the longwave flux are the largest contribution to  $T_{MRT}$ , rendering  $T_s$  of the surrounding built environment the second most important input variable after sun exposure for accurate  $T_{MRT}$  modeling as evidenced in the performance improvement reported here. Spatially explicit  $T_s$  forcing also enhances PET and UTCI calculations, but PET is more sensitive to accurate  $T_s$  input than UTCI.

As for all image based  $T_{MRT}$  models, PanoMRT and RayMan are sensitive to the location of photo acquisition (fisheye image or panorama) in complex urban geometries. Sun exposure may be miscalculated due to pixel misalignment, especially at the transition from horizon limitation to sky and in tree canopies. For some locations, our model evaluation was further impacted by observation procedures and instrumentation setup. MaRTy observations were taken after the thermal panorama was acquired, not concurrently, and in a few instances, one of MaRTy's net radiometers was inadvertently exposed to the sun or shade. Those observational flaws contribute to the unsystematic error in both models and do not bias the model results.

*PanoMRT* is not the first  $T_{MRT}$  model based on thermal photography. Several approaches have been developed in recent years, most of which are restricted to indoor settings. Lee et al. (2019) developed a system using angle factors and an infrared thermal camera to model  $T_{MRT}$  for large stadiums. Their setup overestimated  $T_{MRT}$  by 0.9 °C with  $R^2=0.83$  compared to globe thermometer observations and was subsequently improved to a pan-tilt scanning system (Lee and Jo, 2021). Initial tests of

the system in indoor and longwave-dominated outdoor settings yielded an  $R^2$  of 0.80 (Lee and Jo, 2022). Natephra et al. (2017) integrated thermal images with 3-dimensional Building Information Models (BIMs) to investigate the performance of building envelopes and occupancy comfort levels but did not provide performance statistics. More recently, Acuña Paz y Miño et al. (2020) developed the " $4\pi$ " method to evaluate outdoor radiant environments using photographic high dynamic range (HDR) images and longwave infrared images. The resulting short- and longwave radiance maps yielded  $T_{MRT}$  values within 2 °C of globe temperature readings for 15 observations that were conducted in France and Spain during mostly cloudy winter conditions and at night, so impacts of direct shortwave radiation were minimal. In contrast, Merchant et al. (2022) collected longwave and shortwave panoramas under clear sky, hot, dry conditions in Tempe, Arizona using a SMaRT-SL sensor platform and report a significant improvement over the previous version of the system, which relied on thermal point clouds (Aviv et al., 2021). Their analysis mainly focused on comparing directional short- and longwave panoramas to a 6-directional net radiometer setup but findings suggest that integrating those fluxes into  $T_{MRT}$ would yield accurate results.

*PanoMRT* is in development and has several limitations with respect to shortwave and longwave calculations. The model currently underestimates longwave radiation for sky pixels, i.e.  $T_{MRT}$  is underestimated for sites with high  $f_{SVF}$ . In addition, the threshold to determine sky pixels (4 °C) works well for clear hot dry summer conditions but needs to be adjusted for other meteorological conditions, seasons, and geographic locations. For example, Asawa et al. (2022) manually determined 10 °C and 18 °C as appropriate sky pixel thresholds for a thermal imaging system in Tokyo. Alternatively, sky pixels could be detected automatically from the visible photographs that are used to determine the stitching parameter for the thermal images. Image segmentation approaches using convolutional neural networks to identify sky pixels have gained popularity in recent years and can also handle cloudy conditions (Middel et al., 2019; Nice et al., 2020; Zeng et al., 2018).

At sun-exposed locations, PanoMRT assumes an average albedo of 0.20 for the surrounding surfaces to calculate reflected shortwave radiation. Reflected shortwave contributions are likely overestimated, because the model assumes equal reflection from all solid surfaces, even shaded surfaces, when the location is sun exposed. This yields a "worst-case"  $T_{MRT}$  for sun-exposed locations. Similarly, reflected shortwave radiation is assumed to be zero for shaded locations and therefore underestimated. While this approach simplifies exposure of the complex built environment (e.g. in reality, parallel building walls are not simultaneously exposed), the impact of  $T_{MRT}$  is <1 °C. Longwave radiation in Phoenix is the largest contributor to T<sub>MRT</sub> (Middel and Krayenhoff, 2019), and the impact of sun exposure on surface temperatures is directly captured through the thermal panoramas. Merchant et al. (2022) observed reflected shortwave radiation in the built environment using a SMaRT-SL shortwave array sensor that produces panoramic views of shortwave radiant heat fluxes and found that reflected shortwave radiation can be on the order of 100 Wm<sup>-2</sup> during midday. Most microclimate models that do account for reflection use raytracing and view factors of surface patches to estimate reflected shortwave radiation (Krayenhoff and Voogt, 2007; Lachapelle et al., 2022; Lindberg et al., 2016; Simon et al., 2021). A similar approach could be incorporated into PanoMRT using image segmentation to detect various surface types and assign appropriate radiative and thermal properties to each pixel. Classified surface types would also be required to estimate view factors of buildings and vegetation in each direction to refine the calculation of D (Eqs. (16)–(20)) as implemented by (Lindberg et al., 2008).

Currently, PanoMRT assumes that the thermal panoramas are corrected for emissivity. An appropriate correction for target emissivity is required for accurate  $T_s$  measurements, because  $T_s$  of an object may appear to be emitting more radiation than it really is, for example, a metal bench. Our validation sites were chosen to not have extensive surfaces with low emissivity in the surrounding to minimize the impact of emissivity on the results.

Lastly, PanoMRT cannot model dappled or partial shade because sun exposure is modeled in a true/false fashion with no option to define shade transmissivity. This leads to inaccurate  $T_{MRT}$  estimates under trees with low leaf area density and engineered structures such as photovoltaic canopies and cloth umbrellas. Konarska et al. (2014) measured the transmissivity of total and direct solar radiation through foliated and leafless tree crowns in Göteborg, Sweden and found a wide transmissivity range from 1.3 % to 51.9 %. Results were incorporated into the SOLWEIG model (Lindberg et al., 2008) to improve  $T_{MRT}$  calculations. Transmissivity estimates could be incorporated into PanoMRT by detecting overhead obstructions in the photographs and estimating transmissivity using sky versus non-sky pixels of the obstruction.

PanoMRT is a hybrid modeling approach that relies on  $T_s$  observations to calculate longwave radiation and models shortwave radiation based on the sun position and simple meteorological forcing. As it meets the accuracy requirement of  $\pm$ 5 °C set in the ISO 7726 standard, it has the potential to be used in place of the 6-directional setup, which is considered the gold standard to measure  $T_{MRT}$  but is a major research expense (>\$20 k). Globe thermometers to measure  $T_{MRT}$  are more affordable (\$500) but have a slow response time and require precise heat loss estimates (Vanos et al., 2021). The current thermal panorama setup measures the surroundings in 2–3 min and could be improved further, e.g., by using a FLIR ONE camera attachment for phones that directly captures panoramas without the need for stitching. In summary, PanoMRT constitutes an affordable, practical alternative to current  $T_{MRT}$  acquisition and modeling approaches.

#### 5. Conclusions

Mitigating urban overheating through urban design interventions (e.g., trees, cool pavement) is a top priority of the 21st century for cities around the world. Assessing the impacts of design changes on human thermal exposure requires fine-scale information on radiative heat fluxes in the built environment. We demonstrated the importance of human-centric, spatially explicit  $T_s$  data, i.e., approximated  $T_{ped}$  observations using panoramic thermography, for capturing complex longwave radiation patterns that result from a patchwork of surface types with varying orientation, diurnal sun-exposure, and material characteristics. PanoMRT model results show that  $T_{ped}$  measurements are most important during midday (peak  $T_s$ ) and for shaded locations, because  $T_{ped}$  captures  $T_s$  underneath the shade in contrast to horizontal  $T_s$  from thermal satellite imagery. The use of spatially explicit  $T_s$  as model input improved  $T_{MRT}$  estimates such that they met the accuracy requirement of ±5 °C set in the ISO 7726 standard for heat and cold stress studies.  $T_{MRT}$  modeling errors propagated into thermal comfort index calculations more strongly for PET than UTCI but significantly improved modeling accuracy for both indices, indicating that  $T_{ped}$  is also highly relevant to human thermal comfort assessments.  $T_s$  has long been recognized as key parameter in urban climate, but traditional acquisition methods lack spatial resolution and do not capture pedestrian-relevant surfaces patches. Our work elevates the importance of human-centric, streetlevel  $T_s$  measurements for thermal exposure assessments.

## CRediT authorship contribution statement

AM: Conceptualization, Methodology, Validation, Formal Analysis, Writing, Writing - Original Draft, Writing - Review & Editing, Visualization, Supervision, Project Administration, Funding Acquisition. MH: Software, Methodology, Validation, Writing - Review & Editing. FAS: Investigation, Data Curation, Writing - Review & Editing. AU: Investigation, Data Curation, Writing - Review & Editing. ESK: Methodology, Validation, Writing - Review & Editing.

#### Data availability

Data will be made available on request.

#### Declaration of competing interest

The authors declare that they have no known competing financial interests or personal relationships that could have appeared to influence the work reported in this paper.

#### Acknowledgments

This research was funded by the National Science Foundation, grant number CMMI-1942805 (CAREER: Human Thermal Exposure in Cities - Novel Sensing and Modeling to Build Heat-Resilience). It was further supported by the Healthy Urban Environment (HUE) initiative (who is grateful for the support from the Maricopa County Industrial Development Authority (MCIDA) Award #AWD00033817). This research was also supported by a Natural Sciences and Engineering Research Council of Canada Discovery Grant to ESK. Any opinions, findings, and conclusions or recommendations expressed in this material are those of the authors and do not necessarily reflect the views of the sponsoring organizations.

#### Appendix A. Supplementary data

Supplementary data to this article can be found online at https://doi.org/10.1016/j.scitotenv.2022.160301.

#### References

- Acuña Paz y Miño, J., Lawrence, C., Beckers, B., 2020. Visual metering of the urban radiative environment through  $4\pi$  imagery. Infrared Phys. Technol. 110, 103463. https://doi.org/10.1016/j.infrared.2020.103463.
- Alhadad, S.B., Tan, P.M.S., Lee, J.K.W., 2019. Efficacy of heat mitigation strategies on core temperature and endurance exercise: a meta-analysis. Front. Physiol. 10, 71. https:// doi.org/10.3389/fphys.2019.00071.
- Asawa, T., Oshio, H., Tanaka, K., 2022. Portable recording system for spherical thermography and its application to longwave mean radiant temperature estimation. Build. Environ. 222, 109412. https://doi.org/10.1016/J.BUILDENV.2022.109412.
- Aviv, D., Guo, H., Middel, A., Meggers, F., 2021. Evaluating radiant heat in an outdoor urban environment: resolving spatial and temporal variations with two sensing platforms and data-driven simulation. Urban Clim. 35, 100745. https://doi.org/10.1016/j.uclim. 2020.100745.
- Blazejczyk, K., Epstein, Y., Jendritzky, G., Staiger, H., Tinz, B., 2012. Comparison of UTCI to selected thermal indices. Int. J. Biometeorol. 56, 515–535. https://doi.org/10.1007/ s00484-011-0453-2.
- Broadbent, A.M., Declet-Barreto, J., Krayenhoff, E.S., Harlan, S.L., Georgescu, M., 2022.

  Targeted implementation of cool roofs for equitable urban adaptation to extreme heat.

  Sci. Total Environ. 811. https://doi.org/10.1016/j.scitotenv.2021.151326.
- Chen, L., Ng, E., 2012. Outdoor thermal comfort and outdoor activities: a review of research in the past decade. Cities 29, 118–125.
- Clark, S.S., Chester, M.V., Seager, T.P., Eisenberg, D.A., 2019. The vulnerability of interdependent urban infrastructure systems to climate change: could Phoenix experience a Katrina of extreme heat? Sustain. Resilient Infrastruct. 4, 21–35. https://doi.org/10.1080/23789689.2018.1448668.
- Colter, K.R., Middel, A.C., Martin, C.A., 2019. Effects of natural and artificial shade on human thermal comfort in residential neighborhood parks of Phoenix, Arizona, USA. Urban For. Urban Green. 44. https://doi.org/10.1016/j.ufug.2019.126429.
- Crank, P.J., Middel, A., Wagner, M., Hoots, D., Smith, M., Brazel, A., 2020. Validation of seasonal mean radiant temperature simulations in hot arid urban climates. Sci. Total Environ. 749. https://doi.org/10.1016/j.scitotenv.2020.141392.
- Dunne, J.P., Stouffer, R.J., John, J.G., 2013. Reductions in labour capacity from heat stress under climate warming. Nat. Clim. Chang. 3, 563–566. https://doi.org/10.1038/nclimate1827.
- Fanger, P.O., 1972. Thermal comfort: analysis and applications in environmental engineering. Appl. Ergon. 3, 181. https://doi.org/10.1016/s0003-6870(72)80074-7.
- Fiala, D., Havenith, G., Bröde, P., Kampmann, B., Jendritzky, G., 2012. UTCI-Fiala multi-node model of human heat transfer and temperature regulation. Int. J. Biometeorol. 56, 429–441. https://doi.org/10.1007/s00484-011-0424-7.
- Gál, C.V., Kántor, N., 2020. Modeling mean radiant temperature in outdoor spaces, a comparative numerical simulation and validation study. Urban Clim. 32. https://doi.org/10.1016/j.uclim.2019.100571.
- Gasparrini, A., Guo, Y., Hashizume, M., Lavigne, E., Zanobetti, A., Schwartz, J., Tobias, A., Tong, S., Rocklöv, J., Forsberg, B., 2015. Mortality risk attributable to high and low ambient temperature: a multicountry observational study. Lancet 386, 369–375.
- bient temperature: a multicountry observational study. Lancet 386, 369–375.
  Häb, K., Ruddell, B.L., Middel, A., 2015. Sensor lag correction for mobile urban microclimate measurements. Urban Clim. 14, 622–635. https://doi.org/10.1016/j.uclim.2015.10.003.
- Höppe, P., 1992. A new procedure to determine the mean radiant temperature outdoors. Wetter und Leb. 44, 147–151.
- Höppe, P., 1999. The physiological equivalent temperature a universal index for the biometeorological assessment of the thermal environment. Int. J. Biometeorol. https://doi.org/10.1007/s004840050118.

- ISO, 1998. ISO 7726, Ergonomics of the Thermal Environment, Instruments for Measuring Physical Quantities. Geneva Int. Stand. Organ. doi:ISO 7726:1998 (E).
- Jay, O., Capon, A., Berry, P., Broderick, C., de Dear, R., Havenith, G., Honda, Y., Kovats, R.S., Ma, W., Malik, A., Morris, N.B., Nybo, L., Seneviratne, S.I., Vanos, J., Ebi, K.L., 2021. Reducing the health effects of hot weather and heat extremes: from personal cooling strategies to green cities. Lancet 398, 709–724. https://doi.org/10.1016/S0140-6736(21)01209-5.
- Jendritzky, G., 1990. Bioklimatische Bewertungsgrundlage der Raume am Beispiel von mesoskaligen Bioklimakarten. Akad f Raumforsch u Landesplanung 114, 7–69.
- Jendritzky, G., de Dear, R., Havenith, G., 2012. UTCI-why another thermal index? Int. J. Biometeorol. https://doi.org/10.1007/s00484-011-0513-7.
- Jenerette, G.D., Harlan, S.L., Stefanov, W.L., Martin, C.L., 2011. Ecosystem services and urban heat riskscape moderation: water, green spaces, and social inequality in Phoenix, USA. Ecol. Appl. 21, 2637–2651. https://doi.org/10.1890/10-1493.1.
- Johansson, E., Thorsson, S., Emmanuel, R., Krüger, E., 2014. Instruments and methods in outdoor thermal comfort studies the need for standardization. Urban Clim. 10, 346–366. https://doi.org/10.1016/j.uclim.2013.12.002.
- Kántor, N., Unger, J., 2011. The most problematic variable in the course of human-biometeorological comfort assessment the mean radiant temperature. Cent. Eur. J. Geosci. 3, 90–100. https://doi.org/10.2478/s13533-011-0010-x.
- Kasten, F., 1980. A simple parameterization of the pyrheliometric formula for determining the Linke turbidity factor. Meteorol. Rundschau 33, 124–127.
- Kasten, F., Young, A.T., 1989. Revised optical air mass tables and approximation formula. Appl. Opt. 28, 4735. https://doi.org/10.1364/ao.28.004735.
- Kjellstrom, T., Crowe, J., 2011. Climate change, workplace heat exposure, and occupational health and productivity in central America. Int. J. Occup. Environ. Health 17, 270–281. https://doi.org/10.1179/107735211799041931.
- Konarska, J., Lindberg, F., Larsson, A., Thorsson, S., Holmer, B., 2014. Transmissivity of solar radiation through crowns of single urban trees-application for outdoor thermal comfort modelling. Theor. Appl. Climatol. 117, 363–376. https://doi.org/10.1007/s00704-013-1000-3.
- Kosaka, E., Iida, A., Vanos, J., Middel, A., Yokohari, M., Brown, R., 2018. Microclimate variation and estimated heat stress of runners in the 2020 Tokyo Olympic Marathon. Atmosphere 9. https://doi.org/10.3390/atmos9050192 (Basel).
- Krayenhoff, S.E., Voogt, J.A., 2007. A microscale three-dimensional urban energy balance model for studying surface temperatures. Bound.-Layer Meteorol. 123, 433–461. https://doi.org/10.1007/s10546-006-9153-6.
- Krüger, E.L., Minella, F.O., Matzarakis, A., 2014. Comparison of different methods of estimating the mean radiant temperature in outdoor thermal comfort studies. Int. J. Biometeorol. 58, 1727–1737. https://doi.org/10.1007/s00484-013-0777-1.
- Kuras, E.R., Richardson, M.B., Calkins, M.M., Ebi, K.L., Hess, J.J., Kintziger, K.W., Jagger, M.A., Middel, A., Scott, A.A., Spector, J.T., Uejio, C.K., Vanos, J.K., Zaitchik, B.F., Gohlke, J.M., Hondula, D.M., 2017. Opportunities and challenges for personal heat exposure research. Environ. Health Perspect. 125. https://doi.org/10.1289/EHP556.
- Lachapelle, J.A., Krayenhoff, E.S., Middel, A., Meltzer, S., Broadbent, A.M., Georgescu, M., 2022. A microscale three-dimensional model of urban outdoor thermal exposure (TUF-Pedestrian). Int. J. Biometeorol. 66, 833–848. https://doi.org/10.1007/s00484-022-02241-1.
- Lee, D.S., Jo, J.H., 2021. Pan-tilt ir scanning method for the remote measurement of mean radiant temperatures at multi-location in buildings. Remote Sens. 13, 2158. https://doi.org/10.3390/rs13112158.
- Lee, D.S., Jo, J.H., 2022. Application of IR camera and pyranometer for estimation of longwave and shortwave mean radiant temperatures at multiple locations. Build. Environ. 207, 108423. https://doi.org/10.1016/j.buildenv.2021.108423.
- Lee, H., Mayer, H., 2016. Validation of the mean radiant temperature simulated by the RayMan software in urban environments. Int. J. Biometeorol. 60, 1775–1785. https:// doi.org/10.1007/s00484-016-1166-3.
- Lee, H., Mayer, H., Schindler, D., 2014. Importance of 3-D radiant flux densities for outdoor human thermal comfort on clear-sky summer days in Freiburg, Southwest Germany. Meteorol. Z. 23, 315–330. https://doi.org/10.1127/0941-2948/2014/0536.
- Lee, D.S., Kim, E.J., Cho, Y.H., Kang, J.W., Jo, J.H., 2019. A field study on application of infrared thermography for estimating mean radiant temperatures in large stadiums. Energy Build. 202, 109360. https://doi.org/10.1016/j.enbuild.2019.109360.
- Li, D.H.W., Yang, L., Lam, J.C., 2012. Impact of climate change on energy use in the built environment in different climate zones a review. Energy 42, 103–112. https://doi.org/10.1016/j.energy.2012.03.044.
- Lin, T.-P., Matzarakis, A., Hwang, R.-L., 2010. Shading effect on long-term outdoor thermal comfort. Build. Environ. 45, 213–221.
- Lindberg, F., Grimmond, C.S.B., 2011. The influence of vegetation and building morphology on shadow patterns and mean radiant temperatures in urban areas: model development and evaluation. Theor. Appl. Climatol. 105, 311–323.
- Lindberg, F., Holmer, B., Thorsson, S., 2008. SOLWEIG 1.0-modelling spatial variations of 3D radiant fluxes and mean radiant temperature in complex urban settings. Int. J. Biometeorol. 52, 697–713
- Lindberg, F., Holmer, B., Thorsson, S., Rayner, D., 2014. Characteristics of the mean radiant temperature in high latitude cities-implications for sensitive climate planning applications. Int. J. Biometeorol. 58, 613–627. https://doi.org/10.1007/s00484-013-0638-y.
- Lindberg, F., Onomura, S., Grimmond, C.S.B., 2016. Influence of ground surface characteristics on the mean radiant temperature in urban areas. Int. J. Biometeorol. 60, 1439–1452. https://doi.org/10.1007/s00484-016-1135-x.
- Luber, G., McGeehin, M., 2008. Climate change and extreme heat events. Am. J. Prev. Med. 35, 429–435. https://doi.org/10.1016/j.amepre.2008.08.021.
- Matzarakis, A., Rutz, F., Mayer, H., 2010. Modelling radiation fluxes in simple and complex environments: basics of the RayMan model. Int. J. Biometeorol. 54, 131–139. https:// doi.org/10.1007/s00484-009-0261-0.
- Merchant, C., Meggers, F., Hou, M., Aviv, D., Schneider, F.A., Middel, A., 2022. Resolving radiant: combining spatially resolved longwave and shortwave measurements to improve the understanding of radiant heat flux reflections and heterogeneity. Front. Sustain. Cities, 82 https://doi.org/10.3389/FRSC.2022.869743.

- Middel, A., Krayenhoff, E.S., 2019. Micrometeorological determinants of pedestrian thermal exposure during record-breaking heat in Tempe, Arizona: introducing the MaRTy observational platform. Sci. Total Environ. 687, 137–151. https://doi.org/10.1016/j. scitotenv.2019.06.085.
- Middel, A., Selover, N., Hagen, B., Chhetri, N., 2016. Impact of shade on outdoor thermal comfort—a seasonal field study in Tempe, Arizona. Int. J. Biometeorol. 60, 1849–1861. https://doi.org/10.1007/s00484-016-1172-5.
- Middel, A., Lukasczyk, J., Maciejewski, R., 2017. Sky view factors from synthetic fisheye photos for thermal comfort routing—a case study in Phoenix, Arizona. Urban Plan. 2, 19–30. https://doi.org/10.17645/up.v2i1.855.
- Middel, A., Lukasczyk, J., Maciejewski, R., Demuzere, M., Roth, M., 2018. Sky View Factor footprints for urban climate modeling. Urban Clim. 25, 120–134. https://doi.org/10. 1016/j.uclim.2018.05.004.
- Middel, A., Lukasczyk, J., Zakrzewski, S., Arnold, M., Maciejewski, R., 2019. Urban form and composition of street canyons: a human-centric big data and deep learning approach. Landsc, Urban Plan. 183, 122–132. https://doi.org/10.1016/j.landurbplan.2018.12.001.
- Middel, A., AlKhaled, S., Schneider, F.A., Hagen, B., Coseo, P., 2021. 50 grades of shade. Bull. Am. Meteorol. Soc. 1–35. https://doi.org/10.1175/bams-d-20-0193.1.
- Middel, A., Nazarian, N., Demuzere, M., Bechtel, B., 2022. Urban climate informatics: an emerging research field. Front. Environ. Sci. 10, 532. https://doi.org/10.3389/fenvs.2022. 867434.
- Natephra, W., Motamedi, A., Yabuki, N., Fukuda, T., 2017. Integrating 4D thermal information with BIM for building envelope thermal performance analysis and thermal comfort evaluation in naturally ventilated environments. Build. Environ. 124, 194–208. https://doi.org/10.1016/j.buildenv.2017.08.004.
- Nazarian, N., Krayenhoff, E.S., Bechtel, B., Hondula, D., Paolini, R., Vanos, J., 2022. Integrated assessment of urban overheating impacts on human life. Earth's Futur. https://doi.org/10.1002/ESSOAR.10508877.2.
- Nice, K.A., Wijnands, J.S., Middel, A., Wang, J., Qiu, Y., Zhao, N., Thompson, J., Aschwanden, G.D.P.A., Zhao, H., Stevenson, M., 2020. Sky pixel detection in outdoor imagery using an adaptive algorithm and machine learning. Urban Clim. 31, 100572. https://doi.org/10.1016/j.uclim.2019.100572.
- Nikolopoulou, M., Lykoudis, S., 2006. Thermal comfort in outdoor urban spaces: analysis across different European countries. Build. Environ. 41, 1455–1470. https://doi.org/10. 1016/j.buildenv.2005.05.031.

- Potchter, O., Cohen, P., Lin, T.P., Matzarakis, A., 2018. Outdoor human thermal perception in various climates: a comprehensive review of approaches, methods and quantification. Sci. Total Environ. https://doi.org/10.1016/j.scitotenv.2018.02.276.
- Russo, S., Dosio, A., Graversen, R.G., Sillmann, J., Carrao, H., Dunbar, M.B., Singleton, A., Montagna, P., Barbola, P., Vogt, J.V., 2014. Magnitude of extreme heat waves in present climate and their projection in a warming world. J. Geophys. Res. Atmos. 119, 12500–12512. https://doi.org/10.1002/2014JD022098.
- Simon, H., Sinsel, T., Bruse, M., 2021. Advances in simulating radiative transfer in complex environments. Appl. Sci. 11, 5449. https://doi.org/10.3390/app11125449.
- Stewart, I.D., Oke, T.R., 2012. Local climate zones for urban temperature studies. Bull. Am. Meteorol. Soc. 93, 1879–1900. https://doi.org/10.1175/BAMS-D-11-00019.1.
- Stewart, I.D., Krayenhoff, E.S., Voogt, J.A., Lachapelle, J.A., Allen, M.A., Broadbent, A.M., 2021. Time evolution of the surface urban heat island. Earth's Futur. 9. https://doi.org/ 10.1029/2021EF002178.
- Steyn, D.G., 1980. The calculation of view factors from fisheye-lens photographs: research note. Atmosphere-Ocean https://doi.org/10.1080/07055900.1980.9649091.
- Vanos, J.K., Rykaczewski, K., Middel, A., Vecellio, D.J., Brown, R.D., Gillespie, T.J., 2021. Improved methods for estimating mean radiant temperature in hot and sunny outdoor settings. Int. J. Biometeorol. https://doi.org/10.1007/s00484-021-02131-y.
- VDI, 1994. VDI 3789 Part 2: environmental meteorology, interactions between atmosphere and surfaces; calculation of the short-and long wave radiation. VDI Guide.
- Willmott, C.J., 1982. Some comments on the evaluation of model performance. Bull. Am. Meteorol. Soc. 63, 1309–1369.
- Xia, Y., Li, Y., Guan, D., Tinoco, D.M., Xia, J., Yan, Z., Yang, J., Liu, Q., Huo, H., 2018. Assessment of the economic impacts of heat waves: a case study of Nanjing, China. J. Clean. Prod. 171, 811–819. https://doi.org/10.1016/j.jclepro.2017.10.069.
- Zander, K.K., Botzen, W.J.W., Oppermann, E., Kjellstrom, T., Garnett, S.T., 2015. Heat stress causes substantial labour productivity loss in Australia. Nat. Clim. Chang. 5, 647–651. https://doi.org/10.1038/nclimate2623.
- Zeng, L., Lu, J., Li, W., Li, Y., 2018. A fast approach for large-scale Sky View Factor estimation using street view images. Build. Environ. 135, 74–84. https://doi.org/10.1016/j. buildenv.2018.03.009.